

NUMERICAL ANALYSIS OF A ROTATING CYLINDER WITH SPANWISE DISCS

N. Thouault*, C. Breitsamter*, Jost Seifert**, C. Badalamenti[§], S.A. Prince[§] and N.A. Adams*

*Institute of Aerodynamics, Technische Universität München
Boltzmannstrasse 15, 85748, Garching, Germany

**Bauhaus Luftfahrt e. V.
Lyonel-Feininger-strasse 28, 80807 Munich, Germany

[§]Center for Aeronautics, City University
London, EC1V 0HB, UK

Keywords: *Rotating Cylinder, Vortex Shedding, Spanwise Discs, URANS*

Abstract

The aerodynamic characteristics of a rotating cylinder in cross-flow are investigated by means of Unsteady Reynolds Averaged Navier-Stokes simulations. For a cylinder configuration with endplates, the numerical simulations match the experimental trend for the force coefficients and the Strouhal number. Design parameters are studied including the ratio of circumferential-cylinder-velocity-to-freestream-velocity (α), the endplate diameter ratio and the cylinder aspect ratio. The incoming flow separates on each endplate edge and rolls up into two tip vortices that merge downstream. They impact considerably on the configuration performance particularly at high α . The tip vortices influence the cylinder flow topology especially for low aspect ratio cylinders with small endplates. Finally, a cylinder configuration with spanwise discs is investigated for $\alpha < 3.4$. The streamwise velocity component increases between the boundary layers of two facing discs thereby decreasing the effective spinning ratio. At the corner, the cylinder boundary layer thickness is reduced due to the radial flow component occurring on the disc. Further, adding spanwise discs decreases the strength of the tip vortices. The combination of these three effects leads to a drag reduction at high α compared to a cylinder configuration without spanwise discs.

1 Introduction

Known as the “Magnus effect”, lift is created on a cylinder rotating in a passing flow [1]. The magnitude of the lift force and the corresponding wake flow topology depends on the ratio of cylinder circumferential velocity V_R to freestream velocity V_∞ (or spinning ratio α). Two-dimensional numerical simulations at low Reynolds numbers (in most cases $Re = V_\infty D / \nu \leq 1000$) have evidenced several shedding regimes depending on the spinning ratio. For $\alpha = 0$, a Von Kármán type of vortex shedding has been observed [7-10]. As the spinning ratio increases, the cylinder wake is deflected and features an alternate vortex shedding. The amplitude of the pressure fluctuations in the wake is reduced as α rises [4]. The vortex shedding stops for $\alpha = \alpha_I$. For instance, Stojković et al [8-9] have found numerically that $\alpha_I = 1.9$ for a Reynolds number based on the cylinder diameter of $Re = 200$. The value of α_I depends on Re . Between $\alpha_I \leq \alpha \leq \alpha_{II}$, a steady-state flow has been found ($\alpha_{II} = 4.35$ for $Re = 200$ [9]). A further increment of α leads to a second shedding mode ($\alpha_{II} < \alpha < \alpha_{III}$) characterized by a single vortex shed from the cylinder upstream moving wall ($\alpha_{III} = 4.6$ for $Re = 200$ [9]). In this case, the aerodynamic loads feature a significant amplitude associated with a low frequency (the corresponding Strouhal

number, is one order of magnitude lower than that of the first shedding mode). For $\alpha \geq \alpha_{III}$, the flow reaches again a steady-state [7-9].

Recently, Badalamenti and Prince have performed experimental investigations on a rotating cylinder mounted with endplates [3-4]. The effect of the endplate diameter D_e was evaluated for various spinning ratios. Some of the main conclusions of this experimental work are as follows: large endplate diameters generate significant lift coefficients at high α . However, the power required increases. Relatively low efficiency was found for all configurations tested in terms of lift-to-drag ratio ($L/D < 7$). The lift-to-drag ratio reaches a maximum for a spinning ratio of $\alpha \approx 2$. Total pressure measurements in the cylinder wake indicate that the endplate diameter has a strong effect on the tip vortices (e.g. spanwise position, radius of the vortex core) thereby affecting the drag coefficient C_D and the lift coefficient C_L .

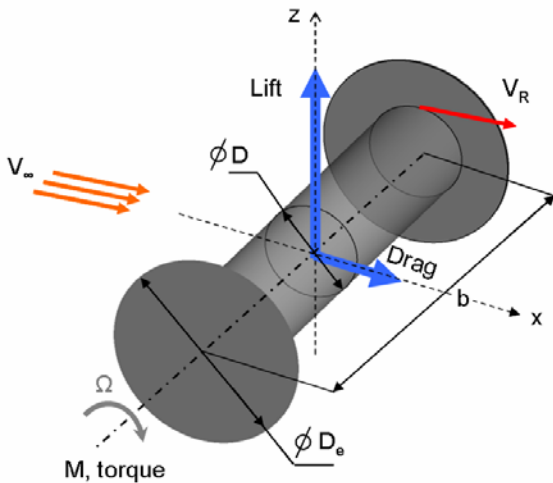


Fig. 1 Sketch of the relevant parameters

Further, experimental investigations on a variety of cylinder arrangements with spanwise discs were conducted by A. Thom in the 1930's [2]. Installing large discs along a cylinder span was found to provide L/D up to 35. Spanwise discs have a considerable influence on C_D . A drag minimum was obtained for $\alpha = 2$ for a cylinder without discs. Contrary, this drag minimum was shifted to $\alpha = 7$ for a cylinder mounted with spanwise discs of spacing-to-diameter ratio of $s = 3/4$. In this particular case, "negative drag" was measured at relatively low Reynolds numbers (around $Re = 6.3 \times 10^3$) and high spinning ratios

($\alpha \approx 7$). A configuration with such performance could constitute a possible alternative for small Unmanned Air Vehicles (UAV) or for small transport vehicles. Current Computational Fluid Dynamics (CFD) methods may offer a way to re-examine the results of Thom and can possibly provide an explanation of the phenomena involved [2].

No numerical simulations of cylinders with discs or endplates have been found in the literature. Comparison of CFD results with experimental data is therefore required to assess the predictive capabilities of state-of-the-art CFD methods for such cases. The experimental setup of Badalamenti and Prince will be first numerically modelled. Unsteady Reynolds Averaged Navier-Stokes (URANS) simulations will be carried out and compared to the experimental data. Then, additional design sensitivity will be provided for relevant parameters described in Fig. 1 including the spinning ratio, $\alpha = V_R/V_\infty = \Omega D/(2V_\infty)$, the cylinder aspect ratio, $A = b/D$ and the endplate (or disc) diameter ratio, D_e/D . Finally, simulation results of a cylinder mounted with spanwise discs will be analyzed.

2 Assessment of CFD predictions

In this section, the setup of the previous experimental investigations [3-4] is briefly described. The numerical method is detailed and a comparison is made with experimental data for a cylinder configuration with endplates.

2.1 Experimental setup

The experimental investigations were conducted at City University London. A detailed description of the setup, the test parameters and the results is available in the work of Badalamenti and Prince [3-4]. The wind tunnel test section dimensions are 1.15m x 0.89m x 1.5m (width x height x length). The cylinder aspect ratio is $A = 5.1$ corresponding to a span of $b = 0.45$ m and a diameter of $D = 0.0889$ m. Endplates of various diameters were tested between $1.1 \leq D_e/D \leq 3$. Force measurements and total pressure measurements in the cylinder

wake were realized. Power spectra of wake pressure measurements were obtained to evaluate dominant frequencies (or Strouhal numbers St) related to vortex shedding phenomena described previously [4]. Results over a wide range of spinning ratios ($0 \leq \alpha \leq 8$) were gathered. The range of Reynolds number investigated was $1.8 \times 10^4 < Re < 9.6 \times 10^4$ corresponding to freestream velocities of $3 \text{ m/s} < V_\infty < 16.5 \text{ m/s}$. Note that the incoming freestream velocity was reduced to obtain high spinning ratios.



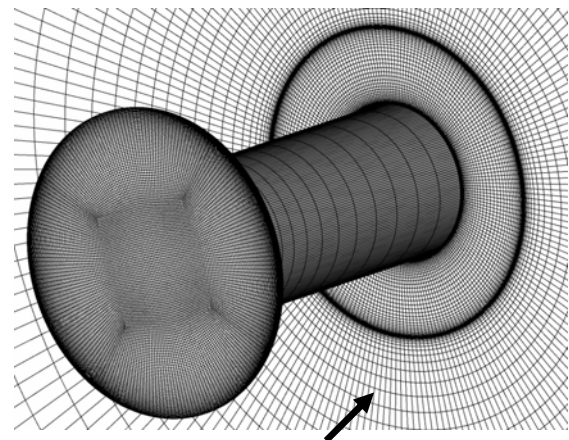
Fig. 2 Cylinder installed in the low-speed wind tunnel [3] at City University London

2.2 Numerical setup

2.2.1 Numerical method

The experimental setup previously described has been reproduced numerically. Several geometrical approximations have been made: the wind tunnel, the chamfer on the outer part of the endplate (11 deg), the support struts and the motor/dummy motor are not modelled. These approximations have been made to reduce the geometrical complexity to obtain a high quality mesh and to decrease the required computational effort for a study of parameters. The mesh has been constructed with ICEM CFD based on a multi-block approach. Note that the mesh is exported as “unstructured” to be used by the solver. A domain of O-topology type is created around the geometry. Similarly as in Ref. [10], the domain diameter is $100 D$. In the spanwise direction, the domain size is of 10

cylinder spans, $10 b (\approx 50 D)$. To further reduce the computational effort, only half of the cylinder is modelled and a symmetry plane is used at the mid-span ($y/(b/2) = 0$). An inlet boundary condition is set on the front part of the domain with a prescribed velocity and turbulence intensity of 1%. On the rear part of the domain, an opening boundary condition [5] is imposed with a relative pressure of 0 Pa, averaged on the entire domain outlet. On the opposite side of the domain, a symmetry boundary condition is also used.



Symmetry plane at $y/(b/2) = 0$

Fig. 3 Surface mesh on the half cylinder with an endplate of diameter $D_e = 2D$

URANS simulations are performed using the commercially available flow simulation software ANSYS CFX that uses an implicit element-based finite volume method. A full second order discretization of the convective term is used throughout all simulations. For the temporal discretization a second order backward Euler scheme is used. All the calculations are performed incompressible. Fully turbulent calculations are carried out using the $k-\omega$ Shear-Stress-Transport (SST) turbulence model of Menter [6]. Indeed, calculations using a transition model based on empirical correlations require significant computational resources and strong mesh constraints [5], inadequate for a study of parameters. Maximal-residuals (momentum and turbulence quantities) are converged to less than 5×10^{-4} . For $\alpha < 3.5$, approximately 400 CPU hours are consumed to obtain a converged solution. The calculations

are performed using 8 nodes on the HLRB2 at the Leibniz supercomputing center (LRZ, Garching near Munich, Germany).

An initial solution is needed for the unsteady run. This solution is obtained with a steady-state RANS simulation at the targeted spinning ratio, α_0 , and the targeted Reynolds number. A perturbation function is applied to trigger the flow unsteadiness. A time dependent rotation speed (or spinning ratio) is defined on the surface of the cylinder for this purpose (Eq. 1). During the application of the perturbation, t_p , the spinning ratio differs from the targeted α_0 by a factor of $(1+f)$. When $t > t_p$, the step function cancels and $\alpha = \alpha_0$. This perturbation has been found suitable to trigger properly the flow unsteadiness.

$$\alpha(t) = \alpha_0 \left[1 + f * \text{step}\left(\frac{t_p - t}{t_p}\right) \right] \quad (1)$$

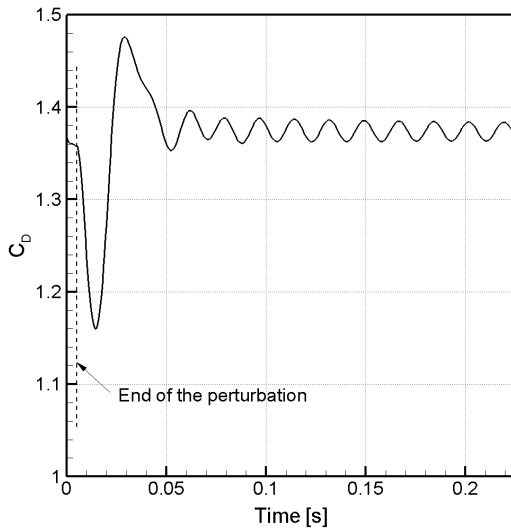


Fig. 4 Time history of the drag coefficient obtained for $\alpha = 2$, $V_\infty = 12$ m/s and $\Omega = 547$ rad/s ($Re = 7.1 \times 10^4$)

A time history of the drag coefficient is presented in Fig. 4 for $\alpha = 2$. The simulation is converged after a computational time of about $t = 0.1$ s. For $\alpha = 2$, oscillations of small amplitude are observed for the lift and drag coefficients contrary to lower spinning ratios. The force coefficients given in this paper are time-averaged over multiple periods of shedding (in the case of alternate vortex shedding, $\alpha \leq 2$). For approximately $2 < \alpha \leq 3.4$ the calculation reaches a quasi-steady state after the

perturbation application with negligible variation of the force coefficients. In the present study, no results are reported for $\alpha > 3.4$.

2.2.2 Grid-dependence study

A grid dependence study has been carried out for $\alpha = 2$, $Re = 7.1 \times 10^4$, $D_e/D = 2$ and $A = 5.1$. Numerous steady-state simulations have first been undertaken to improve the grid sensitivity at low computational cost. The circumferential and spanwise nodes distributions have the most influence on the aerodynamic coefficients.

Direction	Coarse	Medium	Fine
Circumferential	184	212	248
Spanwise	29	36	42
Normal	54	60	68
Total ($\times 10^6$)	1.5	2.0	2.7

Table 1 Details of the grids used

	Coarse	Medium	Fine	Exp.
C_L	5.203	5.190	5.173	4.68
C_D	1.384	1.376	1.370	1.06
St	0.41	0.42	0.43	-

Table 2 Comparison of aerodynamic coefficients for various grid levels ($\alpha = 2$, $Re = 7.1 \times 10^4$, $A = 5.1$ and $D_e/D = 2$)

A grid-resolution study is addressed in this section for unsteady simulations. Three mesh densities are investigated: a coarse grid of 1.5×10^6 nodes, a medium grid of 2.0×10^6 nodes and a fine grid of 2.7×10^6 nodes. Details of the meshes used are given in Table 1. For all variations, the maximum dimensionless wall distance is $y^+_{(max)} = 0.55$ on the cylinder. It has been kept constant for all grids to benefit from the low-Re near wall formulation of the $k-\omega$ SST turbulence model. Contrary, a wall function is used on the endplate with $y^+_{(max)} = 21$ to avoid cells of poor quality at the corner between the cylinder and the endplate. Small differences are observed on the lift and drag coefficients compared to the fine grid. The Strouhal number shows negligible change with respect to a mesh refinement. In the next sections, calculations are performed with the medium grid.

2.3 Comparison to experimental data

In this section, the numerical results are compared to the experimental data for a cylinder configuration with endplates of diameter $D_e = 2D$.

2.3.1 Force coefficients

The lift coefficients predicted by the simulation (num.) shows a good agreement with the experimental data (exp.) for all spinning ratios investigated between $0 \leq \alpha \leq 3.3$, Fig. 5(a).

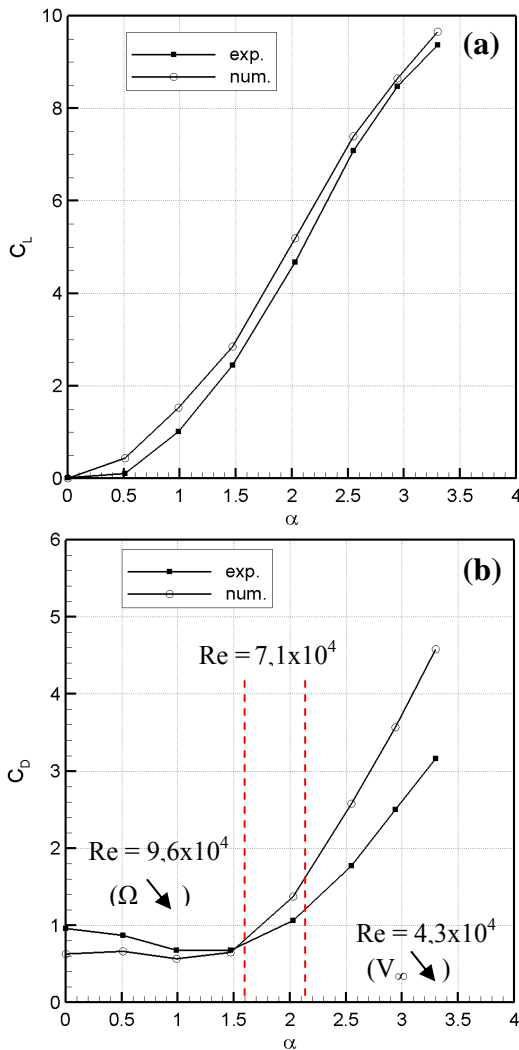


Fig. 5 Comparison of the (a) lift and (b) drag coefficients ($A=5.1$ and $D_e/D = 2$)

The drag coefficients show a satisfactory agreement with experimental data around $\alpha = 1.5$ (Fig. 5(b)). For $0 \leq \alpha < 1$ and $2 < \alpha \leq 3.3$, the numerical results exhibit differences with the measured drag coefficient. Indeed, the portion of laminar flow (not modelled by a fully turbulent calculation) is enhanced due to

reduction of the rotation speed or a decrease of the freestream velocity respectively. Similar conclusions, not presented in this paper, have been drawn for a endplate diameter ratio of $D_e/D = 3$. As previously mentioned, the spinning ratio has experimentally been increased through a reduction of the incoming velocity. For $\alpha > 4$, large differences have been observed between the force measurements and the numerical results. Fully turbulent calculations are clearly not the appropriate approach at low Reynolds number. A fully laminar simulation has been performed at $\alpha = 5.5$ and $Re = 1.7 \times 10^4$ ($V_\infty = 3$ m/s). The simulation results, not presented here, show a better agreement with the experiment. A transition model would help to improve the prediction of the flow at $Re = 1.7 \times 10^4$ and $\alpha = 5.5$. However, the computational requirements would be expensive to perform a parameter variation (due to a small time step and strong mesh constraints [4]). For this reason all the results in this paper concerns $\alpha < 3.4$ (beneath the second shedding mode region).

2.3.2 Wake total pressure

The wake behaviour was in-depth investigated for various endplate diameters, spinning ratios and Reynolds number in Ref. [3]. In this section, a total pressure coefficient (C_{pt}) distribution is plotted at $x/D = 5$ and for $D_e/D = 2$. For $Re = 7.1 \times 10^4$ and $\alpha = 2$, the magnitude and the position of the vortex core is relatively well predicted by the simulation (Fig. 6(a)-(b)).

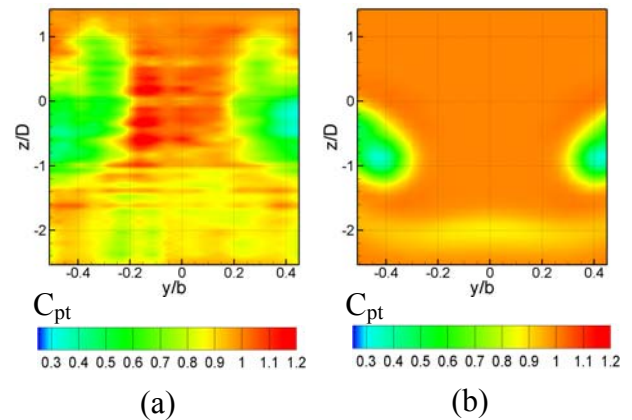


Fig. 6 Total pressure coefficient distribution in the wake at $x/D = 5$: (a) experimental and (b) CFD ($Re = 7 \times 10^4$ and $D_e/D = 2$)

However, the shape of the predicted wake

exhibits significant differences with the experimental results. The geometrical approximations performed have a non negligible impact on the total pressure distribution in the cylinder wake. Recall that the mounting struts, the chamfer on the outer diameter of the endplates, the wind tunnel and the motor/dummy motor have not been reproduced in the numerical setup. As the spinning ratio is increased, the wake is larger and lower total pressures are observed in the core. This trend is predicted by the simulation. The comparison of the simulation results to the experimental data remains however difficult considering the geometrical approximations made.

2.3.3 Strouhal number

The Strouhal numbers predicted by the numerical simulations show a good agreement with the experiment for $\alpha < 1.6$ (Fig. 7). As in the experiment, the numerically obtained St increases with α . A maximum of $St = 0.42$ is found at $\alpha = 2$ ($\approx \alpha_I$ where the first shedding regime stops). No distinct peak was identified experimentally in the power spectra of unsteady pressure measurements for $1.6 < \alpha < 2.8$ [4]. Therefore St is undefined in this region.

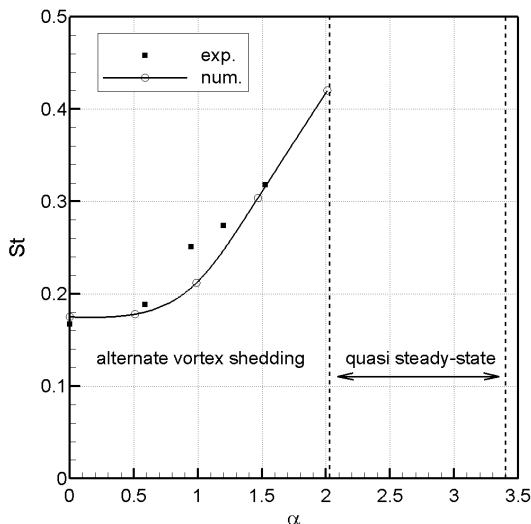


Fig. 7 Comparison of the Strouhal number for various spinning ratios ($D_e/D = 2$ and $A = 5.1$)

For $2 < \alpha \leq 3.4$, the simulations reach a quasi steady-state characterized by negligible variation of all aerodynamic coefficients. The second shedding mode arises numerically around $\alpha_{II} \approx 3.5$ and is characterized by a single vortex shed from the cylinder upstream moving

wall rapidly entrained downstream by the tip vortices thereby increasing their strength (Fig. 8). The corresponding frequency is one order of magnitude lower than in the first shedding regime.

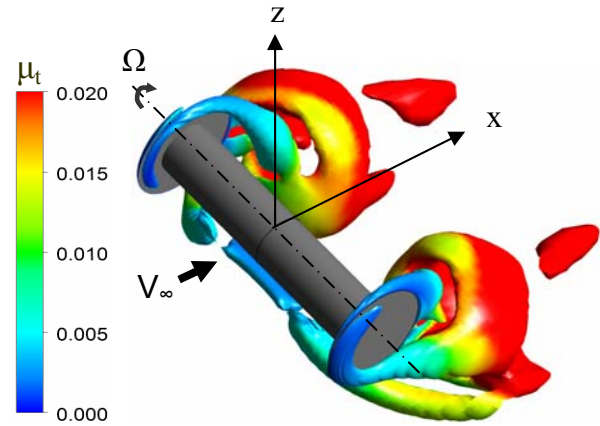


Fig. 8 Flow topology within the second shedding mode region at $\alpha = 4$ and $Re = 7.1 \times 10^4$ (iso-surface of $Q = 3 \times 10^5 \text{ s}^{-2}$ colored by eddy viscosity levels, μ_t)

2.4 First shedding mode flow topology

A sketch of the flow phenomenology is presented in Fig. 9 in the first shedding mode region at $\alpha = 2$ as reference based on precise flow visualizations (e.g. streamlines, vorticity contours). Note that in Fig. 9, the cylinder is upside down. Thus, a positive cylinder rotation (from z to x) generates a lift force in the positive z -direction.

Between the endplates, an alternate vortex shedding is detected due to flow separation occurring on the cylinder surface. The shed vortices rapidly disappear downstream. Again at $\alpha = 2$, the alternate vortex shedding induces force oscillations of small amplitude on the cylinder (Fig. 4). Flow separation occurs on each edge of the endplate. In the cylinder near field, two tip vortices are therefore generated. These vortices merge further downstream to create one vortex of larger core and strength. The wake is deflected by the cylinder rotation. The tip vortices created on each endplate further entrain the flow in the negative z direction. At the corner between the cylinder and the endplate, the vortices generated by flow separation on the cylinder are entrained by the tip vortices consequently affecting their shape.

Additional information on the flow topology is provided in the next sections within a broader range of parameters.

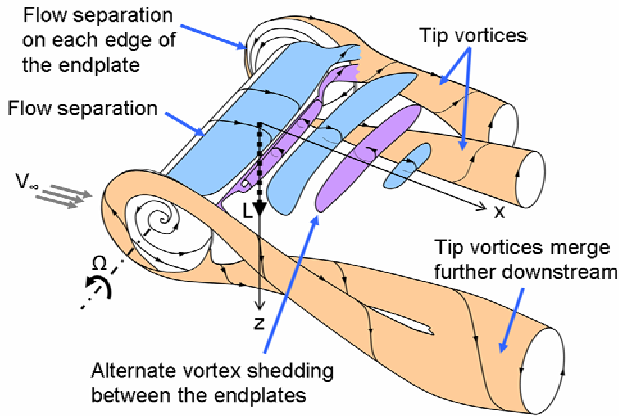


Fig. 9 Flow phenomenology at $\alpha = 2$ ($Re = 7.1 \times 10^4$, $D_e/D = 2$, and $A = 5.1$). The cylinder is upside down

3 Parameter study

In this section, the parameters A , D_e/D and α are varied to increase the configuration design sensitivity.

3.1 Variation of the spinning ratio

In Fig. 14, vortical structures are displayed using an iso-surface of $Q = 3 \times 10^3 \text{ s}^{-2}$ (defined as the difference of the squared absolute value of the vorticity vector with the squared strain rate tensor) and colored by non-dimensional vorticity magnitude, ξ . Recall, the cylinder rotation is positive (from z to x), and the lift force is created in the z direction. As previously stated, flow separation occurs on each edge of the endplates. Considering one endplate, two vortices of identical sign are generated in the near field. As α is increased, the strength of the tip vortices is enhanced (Fig. 14(b)) and the merger of the tip vortices moves upstream (Fig. 14(c)). Large spinning ratios therefore provoke a significant increase of the drag induced by the tip vortices.

Distributions of circumferential pressure coefficient C_p are presented in Fig. 12 for a variety of spinning ratios between $2 \leq \alpha \leq 3.3$. The circumferential coordinate system is

defined in Fig. 10. The circumferential pressure distribution at the cylinder mid-span corresponds to the position $y/(b/2) = 0$. The location $y/(b/2) = 1$ refers to the inboard side of the endplate. A rise of the spinning ratio results in a significant increase of the suction peak (between $\theta = 90^\circ$ and $\theta = 120^\circ$) along the entire span. In addition, the suction peak moves in the positive θ direction on the cylinder outboard part. A negative pressure gradient is observed at $\alpha = 3.3$ (fig. 12(c)) from the mid-span to the endplate. The magnitude of this pressure gradient decreases as α is reduced corresponding to tip vortices of lower strength. As previously said, for $\alpha_I < \alpha < \alpha_{II}$ the flow reaches a quasi-steady state. In this case, two vortices are staying still in the vicinity of the upstream moving wall (Fig. 11) and closed streamlines are observed near the cylinder surface contrary to $\alpha \leq 2$. This phenomenon coincides with the end of the first shedding mode region.

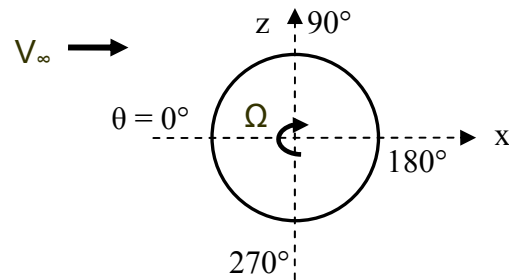


Fig. 10 Circumferential coordinate system

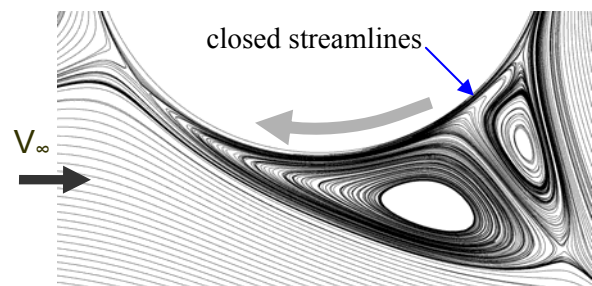


Fig. 11 Streamlines visualization at $y/(b/2)=0$ near the cylinder upstream moving wall ($\alpha = 2.6$, $Re = 4.3 \times 10^4$, $D_e/D = 2$ and $A = 5.1$)

3.2 Variation of the endplate diameter ratio

In this section, the fixed parameters are $A = 5.1$, $\alpha = 2$ and $Re = 7.1 \times 10^4$. The endplate diameter ratio, D_e/D , has a strong influence on the tip

vortices. As D_e is increased, the tip vortices merge further downstream (Fig. 15). For $D_e/D = 4/3$ (Fig. 15(a)), the merger of the tip vortices occurs on the rear part of the endplate.

At a given streamwise position, an increase of the endplate diameter ratio leads to a reduction of the vortex strength (Figs. 15(b) and (c)). Consequently the drag coefficient is reduced (Table 3). The lift coefficient is improved as the endplate diameter ratio is increased. The flow topology around the cylinder depends on D_e/D .

D_e/D	4/3	2	3
C_L	4.90	5.19	5.23
C_D	1.82	1.38	1.07
St	-	0.42	0.39

Table 3 Effect of D_e/D on aerodynamic coefficients ($A = 5.1$, $\alpha = 2$ and $Re = 7.1 \times 10^4$)

The pressure distribution on the cylinder surface is influenced by the endplate diameter ratio. For $D_e/D = 4/3$, the angular location of the suction peak varies along the cylinder span (Fig. 13(a)). In this case, the tip vortex imposes a significant pressure gradient along the cylinder span. For a spanwise location between $0 \leq y/(b/2) \leq 0.75$, a positive pressure gradient is seen from the mid-span to $y/(b/2) = 0.75$. Contrary, in the vicinity of the endplate, a negative pressure gradient is experienced. As already stated, this effect depends significantly on the spinning ratio and the Reynolds number. With an endplate diameter ratio of $D_e/D = 2$, a more homogeneous pressure distribution is achieved along the cylinder span (Fig. 13(b)). For $D_e/D = 3$, a constant pressure distribution is generated on more than 75% of the cylinder span (Fig. 13(c)).

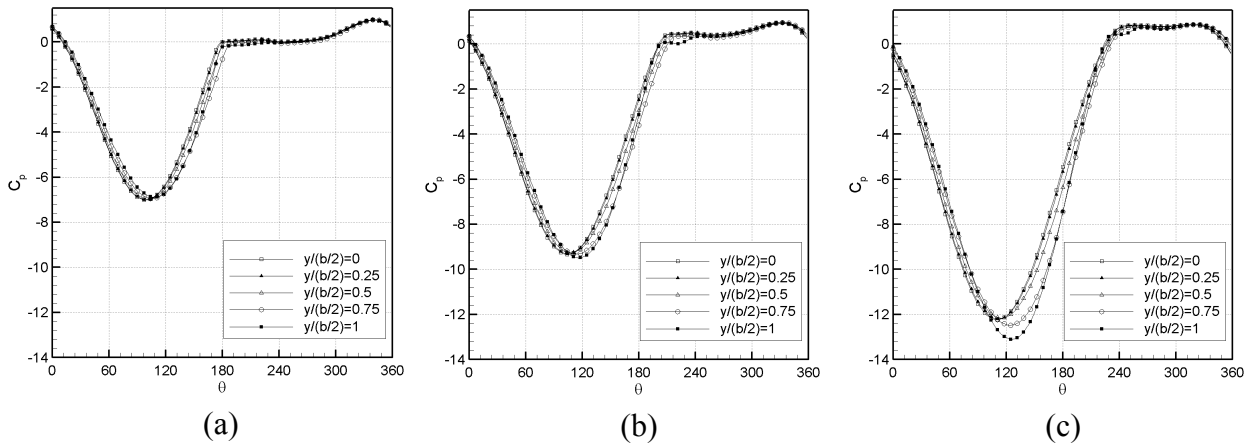


Fig. 12 Influence of the spinning ratio on the circumferential pressure distribution: (a) $\alpha = 2$ ($Re = 7.1 \times 10^4$), (b) $\alpha = 2.6$ ($Re = 4.3 \times 10^4$) and (c) $\alpha = 3.3$ ($Re = 4.3 \times 10^4$). For all cases $D_e/D = 2$ and $A = 5.1$

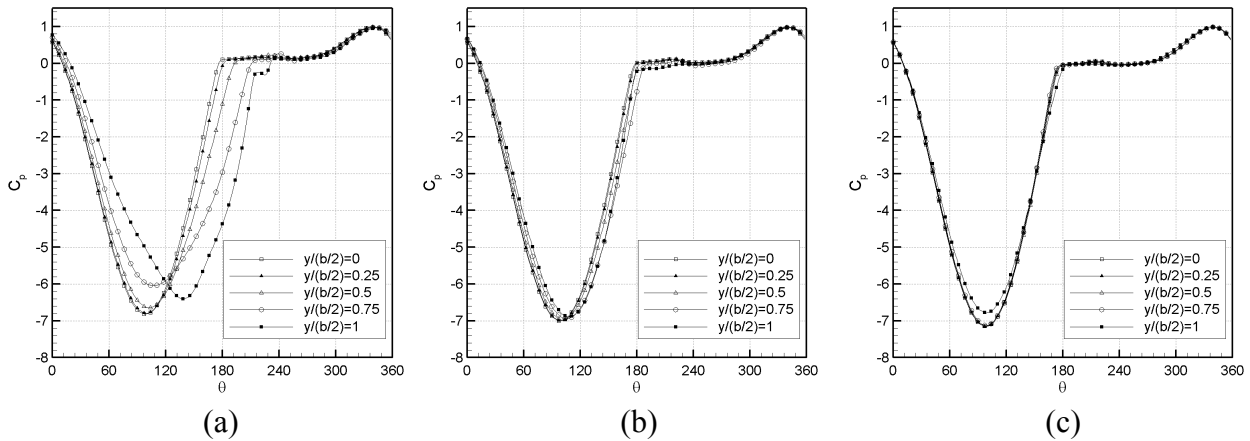


Fig. 13 Influence of the endplate diameter ratio on the circumferential pressure distribution: (a) $D_e/D = 4/3$, (b) $D_e/D = 2$ and (c) $D_e/D = 3$ ($Re = 7.1 \times 10^4$, $A = 5.1$ and $\alpha = 2$)

NUMERICAL ANALYSIS OF A ROTATING CYLINDER WITH SPANWISE DISCS

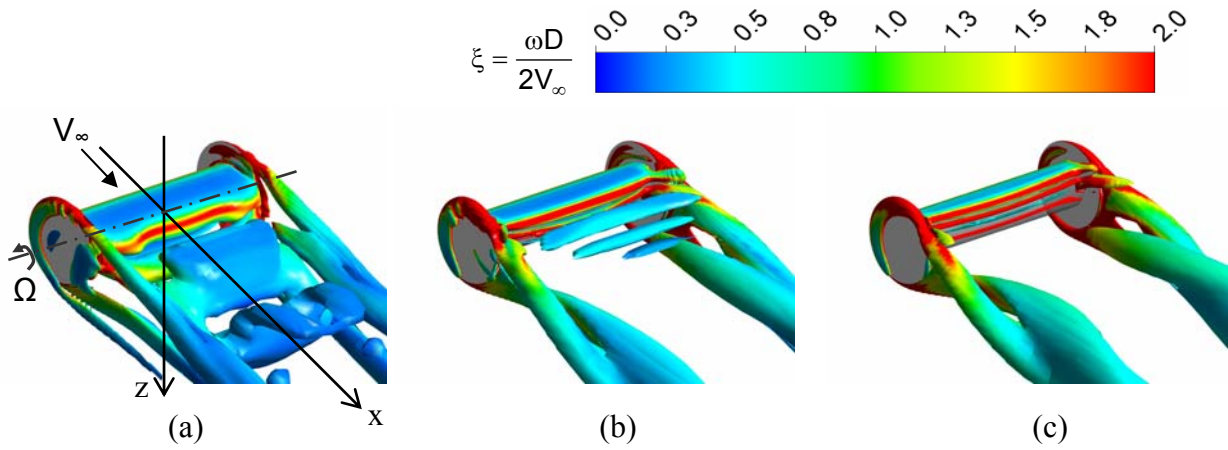


Fig. 14 Vortical structures represented by an iso-surface of $Q = 3 \times 10^3$ for (a) $\alpha = 1$ ($Re = 9.6 \times 10^4$), (b) $\alpha = 2$ ($Re = 7.1 \times 10^4$) and (c) $\alpha = 2.6$ ($Re = 4.3 \times 10^4$). $D_c/D = 2$, and $A = 5.1$. The cylinder is upside down

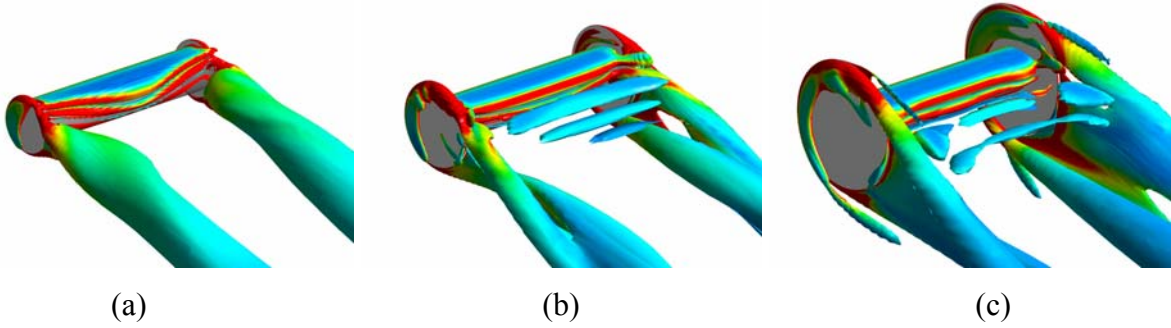


Fig. 15 Vortical structures represented by an iso-surface of $Q = 3 \times 10^3$ for (a) $D_c/D = 4/3$, (b) $D_c/D = 2$ and (c) $D_c/D = 3$ ($\alpha = 2$, $Re = 7.1 \times 10^4$ and $A = 5.1$). The cylinder is upside down

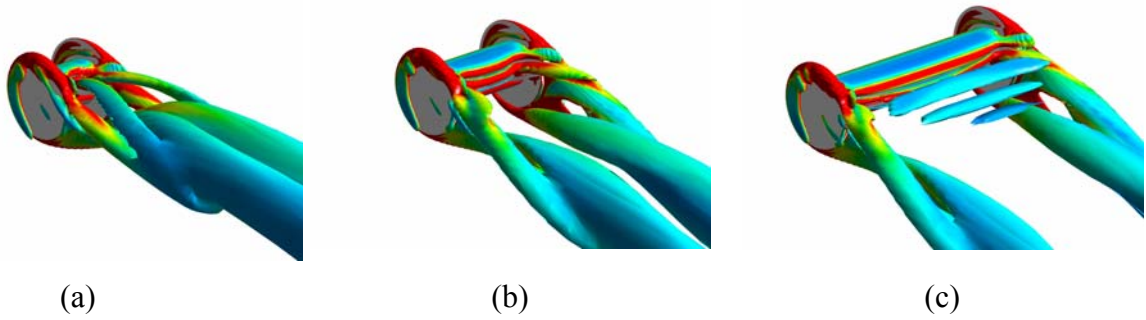


Fig. 16 Vortical structures represented by an iso-surface of $Q = 3 \times 10^3$ for (a) $A = 1.3$, (b) $A = 2.6$ and (c) $A = 5.1$ ($\alpha = 2$, $Re = 7.1 \times 10^4$ and $D_c/D = 2$). The cylinder is upside down

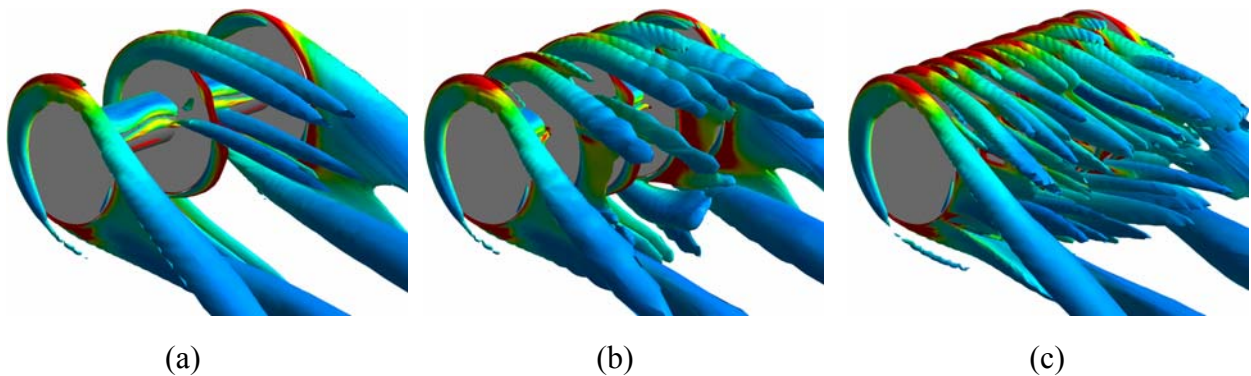


Fig. 17 Vortical structures represented by an iso-surface of $Q = 3 \times 10^3$ for (a) $s = 2.53$ (b) $s = 1.27$ and (c) $s = 0.63$ ($\alpha = 2.4$, $Re = 2.9 \times 10^4$, $A = 5.1$ and $D_c/D = 3$). The cylinder is upside down

Approaching the endplate, a positive pressure gradient is encountered. The pressure gradient along the cylinder span depends on the endplate diameter ratio and is linked to the interaction of the cylinder boundary layer with the endplate boundary layer. Further, at $\alpha = 2$ the numerical simulation reaches a quasi-steady state for $D_e/D = 4/3$. Thus, the Strouhal number is undefined in this case. Contrary, St decreases as the value of D_e/D is raised for $D_e/D \geq 2$. The extension of the first shedding mode region is reduced (α_1 decreases) for cylinders with small endplate diameter ratios.

3.3 Variation of the cylinder aspect ratio

The cylinder aspect ratio is here varied for $\alpha = 2$, $Re = 7.1 \times 10^4$ and $D_e/D = 2$. Reducing the cylinder aspect ratio A provokes a decrease of lift coefficient and a significant increase of the drag coefficient (Table 4). As A is reduced, the influence of the tip vortices on the cylinder pressure distribution is enhanced. Due to a mutual induction, tip vortices of larger strength are created downstream for low aspect ratio cylinders resulting in higher drag and lower lift coefficients (Fig. 16(a)). For $A = 1.3$, the vortices generated by flow separation on the cylinder surface are strongly affected by the tip vortices. In this case, the induction of the tip vortices on these vortices creates tube-like structures connecting the cylinder wake to the tip vortices. Hence, the downstream tip vortex is the result of a merging of three vortices.

A	1.3	2.6	5.1
C_L	4.71	5.09	5.19
C_D	2.96	2.10	1.38
St	-	-	0.42

Table 4 Effect of the aspect ratio on aerodynamic coefficients ($D_e/D = 2$, $\alpha = 2$ and $Re = 7.1 \times 10^4$)

As indicated in Table 4, a quasi-steady flow is found for $A = 1.3$ and $A = 2.6$ (Fig. 16(b)) contrary to the reference configuration ($A = 5.1$, Fig. 16(c)) which features an alternate vortex shedding at $\alpha = 2$. Therefore α_1 increases with the aspect ratio due to a reduced effect of the tip vortices on the cylinder flow.

4 Influence of spanwise discs

In this section, discs are installed along the cylinder span (Fig 18). The effect of the disc-spacing-to-diameter ratio s (or spacing ratio) is evaluated for $A = 5.1$ and $D_e/D = 3$. The numerical method is identical to the one used in section 2.2. Compared to the medium grid of Table 1, a similar node distribution is used in the circumferential and normal direction. However, the spanwise mesh density is increased to keep a similar boundary layer mesh on each disc. A dimensionless wall distance of $y^+_{(max)} = 21$ is achieved on all discs and endplates. Again, only half of the geometry is simulated.

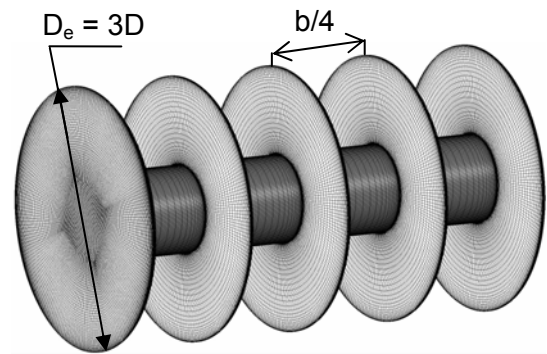


Fig. 18 Surface mesh on a cylinder mounted with spanwise discs of spacing ratio $s = b/(4D) = 1.27$

4.1 Effect of the disc spacing

Adding spanwise discs has a negligible effect on the lift coefficient for $\alpha < 2$ compared to the reference case without spanwise discs. Contrary, a lift reduction occurs for $\alpha > 2.4$, particularly for $s = 1.27$ (Fig. 19 (a)). Further, spanwise discs lead to an increase of the drag coefficient for $\alpha < 2.5$ and a decrease for $\alpha > 2.5$ (Fig. 19 (b)) compared to the reference case, especially for $s = 0.63$. In terms of lift-to-drag ratio, a configuration of $s \leq 1.23$ is more efficient than the reference case at high spinning ratios (Fig. 19(c)). Reducing the spacing ratio induces an increase of the streamwise velocity component between the discs on both the upstream and downstream moving walls compared to the reference case. The streamwise velocity enhancement is particularly significant for $s = 0.63$ between the boundary layers of two facing discs. Therefore, the overall increase of

streamwise velocity between the boundary layers of facing discs causes a decrease of the pressure coefficient along the cylinder span on both upstream and downstream moving walls.

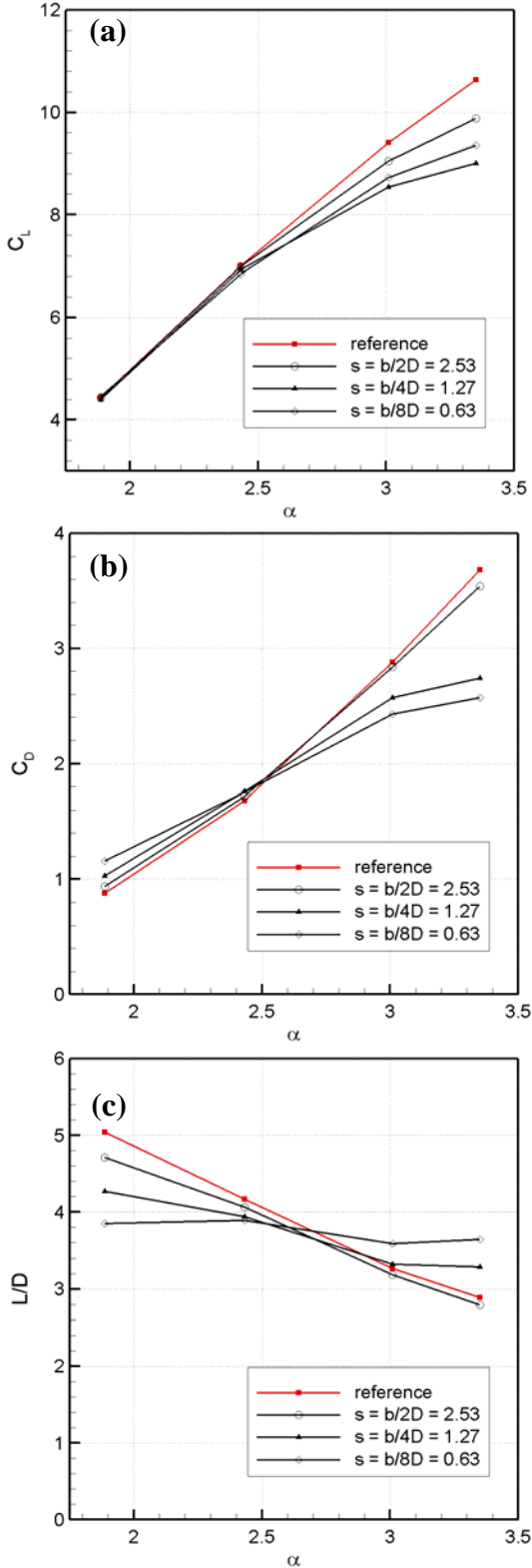


Fig. 19 Comparison of the (a) lift coefficient, (b) drag coefficient and (c) lift-to-drag ratio ($A=5.1$, $De/D = 3$ and $Re = 2.9 \times 10^4$)

Similarly as a channel flow, the streamwise velocity component increases due to the reduced cross section between two spanwise discs. This phenomenon is evidenced in Fig. 20 by streamlines visualization for $\alpha = 3$ in a plane located at $y/(b/2) = 3b/16$ (between two inboard discs for $s = 0.63$). Compared to the reference case, adding a unique disc at mid-span ($s = 2.53$, Fig. 20(a)) has a negligible effect on the overall flow topology. Contrary, for a disc spacing ratio of $s = 0.63$, the flow on the cylinder lower side is clearly entrained through the discs (Fig. 20(b)). Consequently, the vortices on the upstream moving wall are pushed downstream and the wake is less deflected similarly as a decrease of spinning ratio.

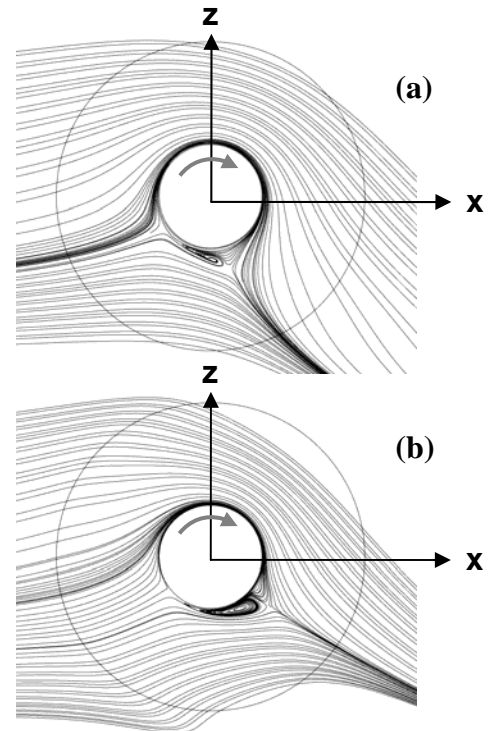


Fig. 20 Streamlines at $y/(b/2)=3b/16$ for (a) $s = 2.53$ and (b) $s = 0.63$ ($De/D = 3$, $\alpha = 3$ and $Re = 2.9 \times 10^4$)

The vortical structures are displayed in Fig. 17 for different spacing ratios. As described previously, separation occurs on each edge of the endplate. Considering a disc installed along the cylinder span, separation occurs also on each of its edges. Consequently, four vortices are generated. In addition, vortices are created at the corner between the cylinder and the spanwise discs on the upstream moving wall.

Depending on the distance between the disc and the endplate, these vortices are entrained by the tip vortices. The strength of the tip vortices decreases as the number of discs increases.

To summarize these findings, a reduction of the disc spacing ratio enhances the streamwise velocity component between the boundary layers of two facing discs. Consequently, a decrease of the effective spinning ratio is induced leading to a drag decrease for $\alpha > 2.5$ and a drag increase for $\alpha < 2.5$. This effect significantly depends also on the Reynolds number. Indeed, the momentum thickness of a turbulent boundary layer differs from that of laminar boundary layer.

4.2 Disc/cylinder boundary layer interaction

As seen previously for $D_e/D = 3$ and $\alpha = 2$ (Fig. 13(c)), the endplate affects the cylinder pressure distribution near the corner. A positive pressure gradient occurs on the cylinder upper side in the vicinity of the endplate. This effect depends strongly on several parameters namely the spinning ratio, the Reynolds number and the diameter ratio.

Installing a middle disc ($s = 2.53$) generates an interaction between the disc and the cylinder boundary layers. A significant radial flow component is observed on the entire disc. On the cylinder upper side and at $x/D = 0$ (Fig. 21), the cylinder boundary layer is entrained by the radial flow in the vicinity of the corner. On the disc outer edge, the boundary layer separates. The separated layer rolls up into a vortex on each side of the middle disc. The disc vortices clearly influence the pressure distribution on the cylinder. Similar effects have been observed for the endplate tip vortices. On both the inboard and outboard side of the endplate, a significant radial flow component occurs also in the endplate boundary layer. However, a single tip vortex is generated on the endplate inboard side (Fig. 17(a)) near the cylinder upper side. Another tip vortex is created near the cylinder lower side and on the outboard side of the endplate.

Due to this radial flow component, the cylinder boundary layer thickness therefore decreases near the endplate and the middle disc. On the

cylinder lower side, a radial flow component is also present on the middle disc. The influence of the middle disc on the cylinder pressure distribution is less pronounced because the flow is separated.

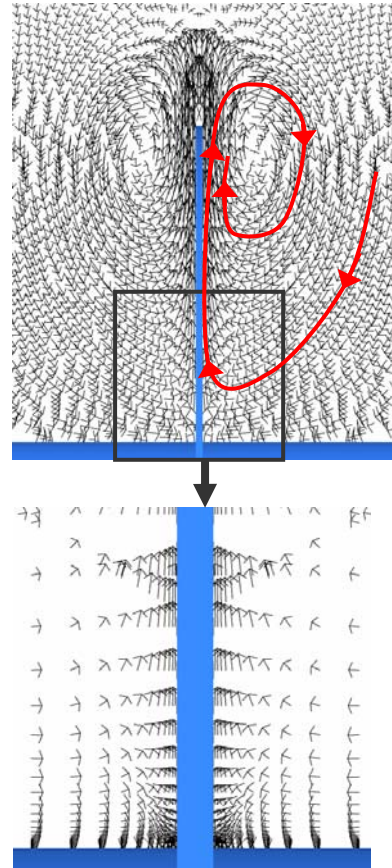


Fig. 21 Velocity vector distribution near the middle disc on the cylinder upper side at $x/D = 0$ ($De/D = 3$, $\alpha = 2.4$, $s = 2.53$ and $Re = 2.9 \times 10^4$)

The flow phenomenology of a rotating cylinder with spanwise discs is represented in Fig. 22 to summarize the present findings.

5 Conclusions

Numerical flow simulations of rotating cylinder configurations have been conducted. The main results are the following:

- 1) The predictive capability of URANS simulations have been assessed for a rotating cylinder mounted with endplates by comparison with the experiment of Badalamenti and Prince [3-4]. Fully turbulent calculations have been performed. For spinning ratios below $\alpha \leq 3.3$, a satisfactory agreement has been found for the

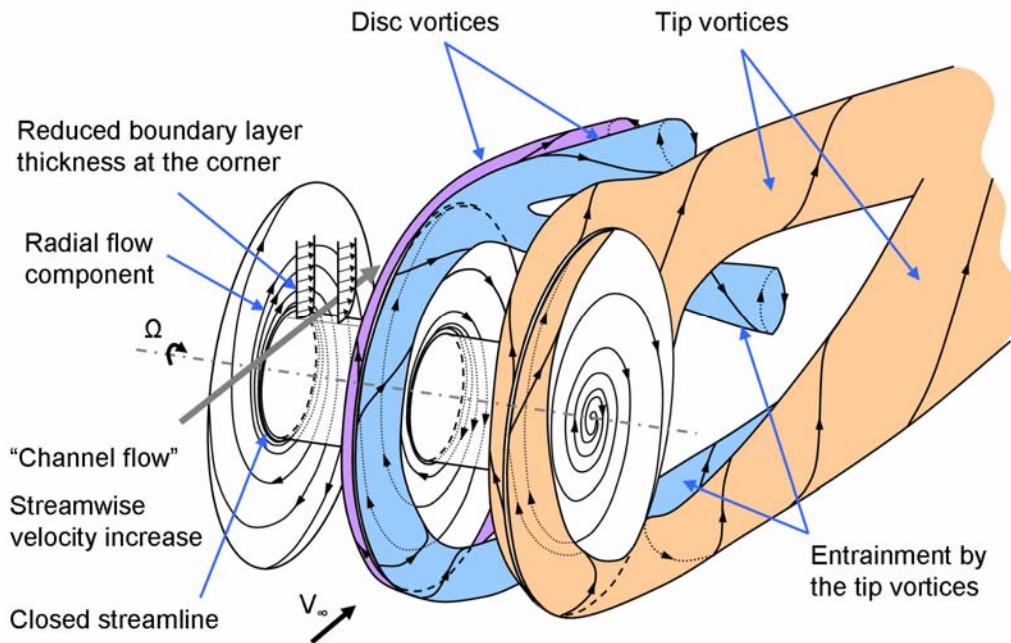


Fig. 22 Flow phenomenology of a rotating cylinder with spanwise discs ($\alpha = 3$, $s = 1.27$ and $D_e/D = 3$)

lift coefficient. Differences have been observed for the drag coefficient at high spinning ratios and low Reynolds number due to a larger portion of laminar flow on the cylinder not captured by a fully turbulent computation. A good agreement has been found for the Strouhal number. The numerical results match well the experimental trend. The flow phenomenology has been described for $\alpha = 2$ within the first shedding mode region.

2) A parameter study has been conducted. The parameters investigated are the cylinder aspect ratio, the endplate diameter ratio, the spinning ratio and the disc-spacing-to-diameter ratio (for a case with spanwise discs). For a configuration without spanwise discs, increasing the endplate diameter leads to a drag reduction and a lift improvement. Cylinders of smaller aspect ratio show higher drag and lower lift. In this case, the tip vortices impact strongly on the cylinder flow topology. Increasing the spinning ratio produces tip vortices of more significant strength thereby enhancing the induced drag. For all variations, the tip vortices affect considerably the configuration performance and are a key design parameter. The spanwise pressure gradient occurring near the endplate depends on the endplate diameter, the spinning ratio, the cylinder aspect ratio and the Reynolds number.

3) The effect of spanwise discs on a rotating cylinder configuration has been assessed within the range of spinning ratios of $1.9 \leq \alpha \leq 3.4$. The streamwise velocity component is enhanced between the boundary layer of two facing discs (compared to a configuration without spanwise discs), particularly for $\alpha > 2.5$. This streamwise velocity rise leads to a flow phenomenology modification (e.g. streamlines, pressure distribution) comparable to a reduction of spinning ratio. This effect significantly depends on the disc spacing ratio and the Reynolds number (laminar/turbulent boundary layer). In addition, a radial flow component on spanwise discs causes a reduction of the cylinder boundary layer thickness at the corner. Further, increasing the number of spanwise discs generates additional vortical structures originating from flow separation on the edges of each disc resulting in a reduction of the strength of the tip vortices compared to a configuration without spanwise discs. The combination of these three effects leads to a drag reduction for $\alpha > 2.5$. The cylinder performance is expected to be improved at higher spinning ratios. Additional work will be conducted to confirm the benefit of spanwise discs for $\alpha > 3.5$. Further simulations will be made to characterize the flow field at high spinning ratios for a cylinder configuration with endplates.

Acknowledgments

The authors would like to thank ANSYS CFX for providing the flow simulation software.

References

- [1] Magnus G. On the Deflection of a Projectile, Possendorf's Annalen der Physik und Chemie, Vol. 88, pp. 804-810, 1853
- [2] Thom A. Effect of Discs on the Air Forces on a Rotating Cylinder, *R & M No. 1623*, 1934.
- [3] Badalamenti C and Prince S A. The Effects of Endplates on a Rotating Cylinder in Crossflow. *AIAA 2008-7063*, 2008.
- [4] Badalamenti C. and Prince S A. Vortex Shedding from a Rotating Circular Cylinder at Moderate sub-critical Reynolds Numbers and High Velocity Ratio, *Proceedings of the 26th ICAS*, Anchorage, USA, 2008.
- [5] Ansys. ANSYS CFX-solver Theory Guide, 2006.
- [6] Menter F R. Two-Equation Eddy-Viscosity Turbulence Models for Engineering Applications. *AIAA Journal*, Vol. 32, No. 8, pp. 1598-1605, 1994.
- [7] Mittal S. and Kumar, B., Flow past a Rotating Cylinder. *Journal of Fluid Mechanics*, vol. 476, pp. 303-334, 2003.
- [8] Stojkovic D, Breuer M and Durst F. Effect of high rotation rates on the laminar flow around a circular cylinder. *Physics of Fluids*, Vol. 14, No. 9, pp. 3160-3178, 2002.
- [9] Stojkovic D, Schön P, Breuer M and Durst F. On the New Vortex Mode Past a Rotating Circular Cylinder. *Physics of Fluids*, Vol. 15, No. 5, pp. 1257-1260, 2003.
- [10] Padriano J C and Joseph D D. Numerical Study of the Steady-State Uniform Flow Past a Rotating Cylinder. *Journal of Fluid Mechanics*, Vol. 557, pp. 191-223, 2006.

Copyright Statement

The authors confirm that they, and/or their company or organization, hold copyright on all of the original material included in this paper. The authors also confirm that they have obtained permission, from the copyright holder of any third party material included in this paper, to publish it as part of their paper. The authors confirm that they give permission, or have obtained permission from the copyright holder of this paper, for the publication and distribution of this paper as part of the ICAS2010 proceedings or as individual off-prints from the proceedings.